

Mid- to Far-Infrared Anisotropic Dielectric Function of HfS₂ and HfSe₂

Ryan A. Kowalski, Joshua Ryan Nolen, Georgios Varnavides, Sebastian Mika Silva, Jack E. Allen, Christopher J. Ciccarino, Dominik M. Juraschek, Stephanie Law, Prineha Narang, and Joshua D. Caldwell

R. A. Kowalski, J. R. Nolen, J. D. Caldwell
Interdisciplinary Materials Science Program, Vanderbilt University, Nashville, TN 37212, USA
E-mail: josh.caldwell@vanderbilt.edu

J. R. Nolen
Photonics Initiative, Advanced Science Research Center, City University of New York, New York, NY 10031, USA

G. Varnavides, C. J. Ciccarino, D. M. Juraschek, P. Narang
John A. Paulson School of Engineering and Applied Sciences, Harvard University, Cambridge, MA 02138, USA

S. M. Silva, S. Law
Department of Materials Science and Engineering, University of Delaware, Newark, DE 19716, USA
E-mail: slaw@udel.edu

J. E. Allen, J. D. Caldwell
Department of Mechanical Engineering, Vanderbilt University, Nashville, TN 37212, USA

D. M. Juraschek
School of Physics and Astronomy, Tel Aviv University, Tel Aviv 69978, Israel

© 2022 Wiley-VCH GmbH

Abstract

The far-infrared (far-IR) remains a relatively underexplored region of the electromagnetic spectrum extending roughly from 20 to 100 μm in free-space wavelength. Research within this range has been restricted due to a lack of optical materials that can be optimized to reduce losses and increase sensitivity, as well as by the long free-space wavelengths associated with this spectral region. Here the exceptionally broad Reststrahlen bands of two Hf-based transition metal dichalcogenides (TMDs) that can support surface phonon polaritons (SPhPs) within the mid-infrared (mid-IR) into the terahertz (THz) are reported. In this vein, the IR transmission and reflectance spectra of hafnium disulfide (HfS₂) and hafnium diselenide (HfSe₂) flakes are measured and their corresponding dielectric functions are extracted. These exceptionally broad Reststrahlen bands (HfS₂: 165 cm^{-1} ; HfSe₂: 95 cm^{-1}) dramatically exceed that of the more commonly explored molybdenum- (Mo) and tungsten- (W) based TMDs ($\approx 5\text{--}10 \text{ cm}^{-1}$), which results from the over sevenfold increase in the Born effective charge of the Hf-containing compounds. This work therefore identifies a class of materials for nanophotonic and sensing applications in the mid- to far-IR, such as deeply sub-diffractive hyperbolic and polaritonic optical antennas, as is predicted via electromagnetic simulations using the extracted dielectric function.

1 Introduction

Historically, research within the far-IR region of the electromagnetic spectrum^[1-3] has been challenging compared to other spectral windows due to the lack of an established optical infrastructure. Spectroscopy in this range can be a difficult task, due to the lack of efficient radiation sources within the so-called “terahertz gap” that extends beyond the range where blackbody sources can provide sufficient power. Despite recent developments to create powerful radiation within this region, accessing solid-state properties at these frequencies remains challenging.^[4-6] Passive optical components in the mid- to far-IR also suffer from undesirable dispersion due to the optic phonon resonances of the material. This dispersion is associated with high absorption losses and optical performance that is strongly frequency dependent, resulting in a non-uniform transmission intensity over the spectral band of interest.^[7] Materials with suitable spectral properties exist, but they all suffer from other challenges. For example, cesium iodide (CsI) has extremely low-energy vibrational modes outside of this spectral range giving rise to suitable transmission,^[8-10] but it is hygroscopic and therefore must be operated under vacuum or kept within other inert atmospheres. While thin polymer coatings can be applied over CsI optics as a protective layer, these induce additional vibrational resonances,

thereby compromising performance.^[11–13] Interest among other materials in this spectral range include indium phosphide (InP) for its potential generation of far-IR radiation^[14] as well as barium (BaTiO₃) and strontium (SrTiO₃) titanate,^[15,16] which are popular ferroelectric materials for microwave electronics. Finally, while these materials provide opportunities for transparent windows, they are still restricted by the diffraction limit, resulting in large sizes for optical components. Alternative materials are therefore widely desired to further advance research efforts in the far-IR. In contrast, reflective optics do not typically suffer from large dispersion like many transmissive components do, yet, the long free-space wavelengths still enlarge the footprint of any optical devices, limiting their functionality and precluding normal incidence excitation or detection in most configurations.

Nanophotonic devices, which confine light to lengths scales below the diffraction limit, can be designed to circumvent such issues. This confinement can be achieved by employing materials supporting light-matter quasiparticles called polaritons.^[2,17] While surface plasmon polaritons have been the focus of intense research over the past couple decades,^[18–21] surface phonon polaritons (SPhPs) offer significantly reduced absorption losses and thus,^[22,23] have been a subject of increased interest. SPhPs are hybrid modes comprised of electromagnetic waves and the coherently oscillating ionic charges in polar dielectric crystals.^[19] An internal electric field generated by polar bonds in the crystal creates an energy splitting between the transverse (TO) and longitudinal (LO) optic phonons, resulting in the so-called Reststrahlen band.^[24,25] Within this band, the material exhibits optically metallic behavior due to the coherent oscillation of these polar charges, giving rise to a negative real part of the permittivity tensor ($\text{Re}(\epsilon_r) < 0$). Due to the negative real part of the permittivity tensor within the Reststrahlen band, SPhPs can be supported at the polaritonic medium–air interface. Therefore, polar dielectric materials with large TO-LO phonon splitting in the mid- to far-IR and THz spectral ranges^[19,26,27] are excellent candidates for devices such as on-chip nanophotonics,^[17,18,28,29] and super-resolution imaging.^[2,30] This work investigates the TMD class of materials, which satisfies the above requirements, but have not been studied in depth in the far-IR.^[31]

TMDs are an emerging group of materials with recent interest stemming from their 2D optical and electronic properties^[32–42] in the visible to near-infrared spectrum. Most research within this material system has focused on the optical properties of group-VIB transition metals such as molybdenum or tungsten disulfides (MoS₂, WS₂)^[43,44] and diselenides (MoSe₂, WSe₂),^[45] with recent focus turning to ditellurides,^[36,40,46] but have mostly neglected the group-IVB dichalcogenides. In particular, Hf-based TMDs have a highly ionic bonding character that, in contrast with group-VIB TMDs, offer the potential for a large TO-LO splitting. The magnitude of the TO-LO splitting is proportional to the Born effective charge (Z_B^*),^[47,48] which gives rise to a very broad Reststrahlen band. Further, Hf-based TMDs tend to have phonons that exist at low IR frequencies due to the larger ion mass. This spectral range has been historically difficult to access because of the previously mentioned phonon dispersion in common optical materials.

The design of nanophotonic structures requires simulations of the electromagnetic response of a material, for which a reli-

able dielectric function is essential.^[31] In this work, we extract the dielectric functions of HfS₂ and HfSe₂ crystals through least-squares fitting of polarized reflectance and transmission measurements collected through Fourier Transform IR (FTIR) micro-spectroscopy. For micron-scale samples, FTIR micro-spectroscopy provides considerable advantages over more conventional approaches, such as variable-angle spectroscopic ellipsometry (VASE) where the collection area is much larger than the typical lateral flake size. Although VASE is independent of intensity, the smaller scale samples can create difficulties in the experimental configuration. Instead, FTIR measurements with an IR microscope provide more flexibility to measure micron-scale samples such as exfoliated 2D materials.^[22,49] This approach has been successfully employed to extract the dielectric function of other 2D materials, such as hexagonal boron nitride (hBN)^[22,49] and orthorhombic α -phase molybdenum trioxide (α -MoO₃).^[50] The hexagonal crystal structure of group-IVB TMDs results in a dielectric tensor that is uniaxial, similar to that of hBN. Therefore, the symmetry of the lattice results in an out-of-plane dielectric tensor component that differs from the in-plane isotropic components $\epsilon_{xx}(\omega) = \epsilon_{yy}(\omega) \neq \epsilon_{zz}(\omega)$. The in-plane TO and LO phonon frequencies of HfS₂ and HfSe₂ have been documented in the past through both IR and Raman spectroscopy.^[51,52] However, the excitation of the TO and LO phonons aligned with the optic axis ($\mathbf{E} \parallel \hat{c}$) is forbidden by symmetry rules at normal incidence,^[53] and therefore determining the full dielectric tensor using available micron-scale flakes in the far-IR has thus far been a significant challenge. Past studies have attempted to assign these values through second-order resonance Raman and two-phonon absorption measurements,^[54,55] however their direct observation through IR reflectance measurements has yet to be demonstrated. Here, we overcome these limitations through polarized reflection at grazing incidence (55°), verifying previously reported values, quantifying the out-of-plane contributions, and providing a model for the full dielectric tensor of Hf-based TMDs in the far-IR. Further, we calculate the Born effective charge for monolayer structures of these compounds from first-principles, providing insight into the origin of the broad Reststrahlen bands of this material class with respect to other TMDs.

2. Results and Discussion

HfS₂ and HfSe₂ are polar van der Waals semiconductors that are thermodynamically stable at room temperature with a distorted octahedral (1T) atomic structure within the $P\bar{3}m1$ space group (**Figure 1a**). The vibrational modes of HfS₂ and HfSe₂ can be predicted from the space group symmetry and are expressed in the irreducible representation as:

$$\Gamma = A_{1g} + E_g + 2A_{2u} + 2E_u \quad (1)$$

where A_{1g} and E_g are Raman-active and A_{2u} and E_u are IR-active vibrational modes. Both A_{2u} and E_u modes consist of transverse and longitudinal components that are parallel and perpendicular to the c -axis, respectively. The bonding between the Hf and chalcogenide atoms gives the structure its strong ionic character, where the conduction and valence bands are comprised

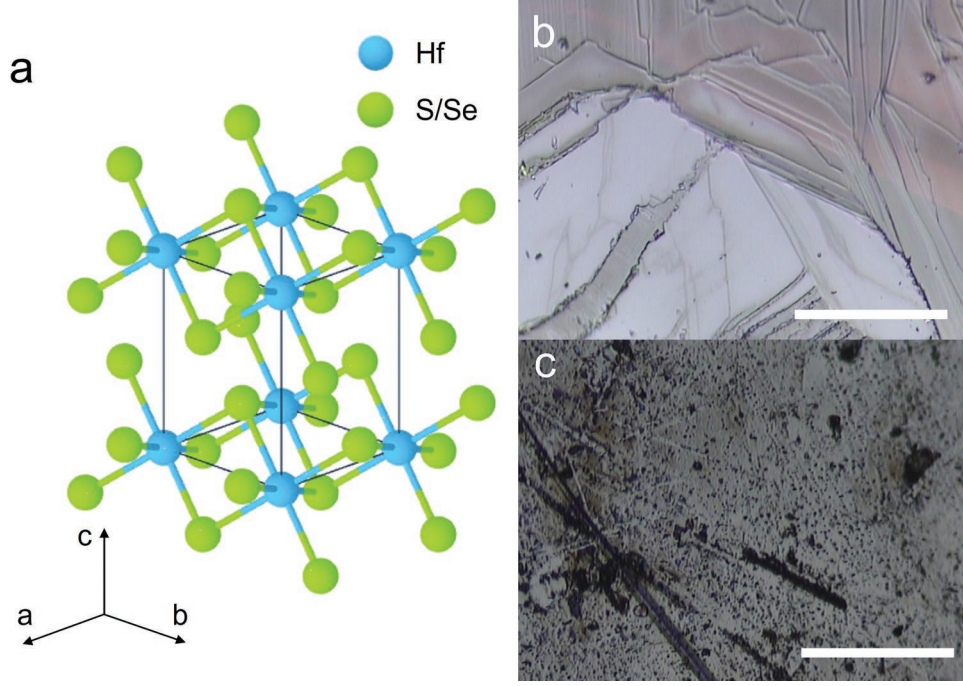


Figure 1. a) Schematic of the HfS₂ and HfSe₂ crystal unit cell.^[57] Micrograph images of b) HfS₂ and c) HfSe₂ flakes. Scale bar is 100 μm .

of Hf-d orbitals and S/Se-p orbitals,^[47] respectively. This is evident from the difference in Pauling electronegativity values that transition between Mo (2.2) and Hf (1.3) in comparison to S/Se (2.4/2.5).^[57] Therefore, the Hf-based TMDs demonstrate a higher degree of ionicity and tend to form more polarized bonds.

2.1. Born Effective Charge Calculations

In bulk 3D polar systems, the Coulomb interaction results in a splitting between the TO and LO phonons within the far-IR leading to a frequency discontinuity near the Γ -point. By contrast, in polar 2D materials, the reduced dimensionality of the Coulomb interaction instead manifests as a slope discontinuity of the frequency bands at the Γ -point. Formally, the non-analytical term correction between the TO (ω_{TO}) and LO (ω_{LO}) frequencies can be given in d dimensions as:^[59]

$$\omega_{\text{LO}}^2 = \omega_{\text{TO}}^2 + V_d(q) \frac{q^2}{\Omega_d} |\hat{\mathbf{q}} \cdot \mathbf{Z}_\alpha|^2 \quad (2)$$

where $\hat{\mathbf{q}}$ is the unit wavevector of the phonon in mode α and $V_d(q)$ and Ω_d are the screened Coulomb interaction and unit cell “volume” in d dimensions, respectively. The mode effective charge vector, \mathbf{Z}_α is given by:

$$\mathbf{Z}_\alpha = \sum_n \frac{Z_n^* \hat{\mathbf{e}}_{\alpha,n}}{\sqrt{M_n}} \quad (3)$$

where Z_n^* is the Born effective charge tensor of atom n , $\hat{\mathbf{e}}_{\alpha,n}$ is the eigenvector of the phonon in mode α and M_n is the atomic mass of atom n where n indexes all the atoms in the unit cell.

Here, we begin our evaluation with the strength of the SPhP interaction in monolayers of HfSe₂ and HfS₂ using first-principles calculations to compute their Born effective charge tensors and contrast them against similar 2D layered compounds, MoS₂ and WSe₂. In the two-dimensional limit, the SPhP of a material becomes a 2D phonon polariton that is equivalent to the 2D LO mode due to its highly confined and evanescent character.^[24,25,59] We start by summarizing the Born effective charges in the corresponding bulk 3D systems (Table 1). The first (last) two rows refer to the Born effective charge on the transition metal (chalcogen) atoms along the in-plane and out of plane directions. Note that the sign of the Born effective charges on the transition metal and chalcogen atoms is flipped for the Hf-based compounds, indicative of the different ionic character of the bond, due to the reduced electronegativity of Hf in comparison to Mo and W. More importantly, the magnitude of both the in-plane and out-of-plane Born effective charges of the Hf-based compounds is several times larger than Mo- or W-containing TMDs. In the monolayer limit, the wavevector dependence of the LO and TO frequencies, following the nonanalytical-term correction given by Equation (2) for 2D is provided in Figure 2. While the shape of the frequency discontinuity near the Γ -point

Table 1. Independent components of Born effective charge tensors for various 3D bulk polar semiconductors.

	MoS ₂	MoSe ₂	WS ₂	WSe ₂	HfS ₂	HfSe ₂
Transition $Z_{xx(yy)}^*$	-1.06	-1.83	-0.59	-1.28	7.67	9.60
Transition Z_{zz}^*	-0.62	-0.99	-0.41	-0.40	1.94	2.18
Chalcogen $Z_{xx(yy)}^*$	0.54	0.90	0.29	0.64	-3.83	-4.80
Chalcogen Z_{zz}^*	0.34	0.45	0.23	0.20	-0.97	-1.09

Data from Kyoto University’s Phonon Database in units of [e].^[58,60]

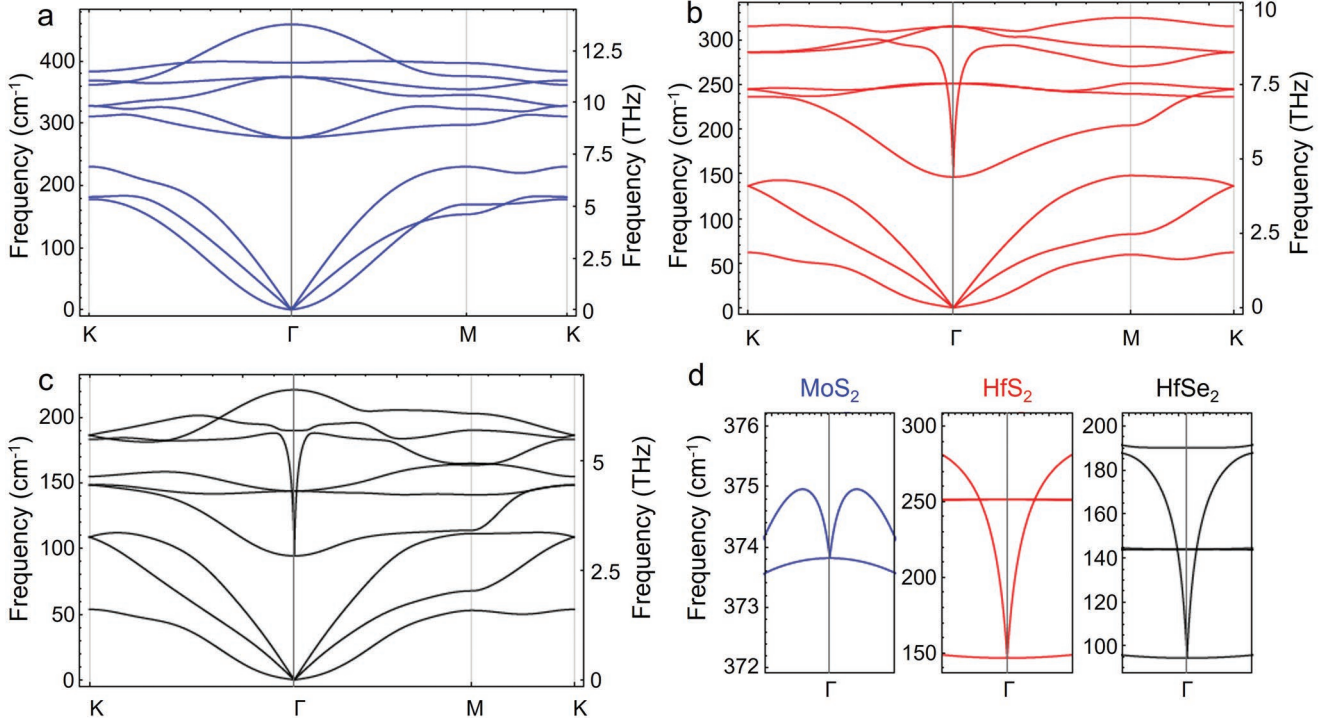


Figure 2. Wavevector dependence of TO-LO “splitting” in 2D polar semiconductors. Phonon dispersion relations for monolayer a) MoS₂, b) HfS₂, and c) HfSe₂. d) Γ -point close-up of the TO-LO frequency slope discontinuity, highlighting the large magnitude difference between the Hf-based compounds and MoS₂.

is similar across all three compounds, the magnitude of the difference between the LO and TO frequencies, which must converge at the Γ -point, is made apparent through the comparison of the Hf-based compounds with that observed for MoS₂. This is directly proportional to the magnitude of the Born effective charge tensor which, consistent with the bulk values in Table 1, we find to be 5–7 times larger in the Hf-based compounds.

2.2. Dielectric Function of HfS₂ and HfSe₂

2.2.1. FTIR Micro-Spectroscopy Reflectance Measurements

The HfS₂ and HfSe₂ samples are free-standing layered crystals (Figure 1b,c) with large thickness non-uniformities, which make the samples less than ideal for large-scale measurement techniques such as traditional FTIR measurements within a bench and IR variable angle spectroscopic ellipsometry (IR-VASE). As stated above, here FTIR micro-spectroscopy is used as this allows for the collection area to be decreased to tens of microns on a side, therefore reducing the non-idealities observed via other methods. The large difference in TO-LO splitting between group-IVB and group-VIB TMDs can be seen by comparing the reflectance spectra from flakes of Hf-based and Mo-/W-based TMDs (Figure 3). The Mo- and W-based samples exhibit very narrow Reststrahlen bands on the order of only a few cm⁻¹, whereas HfS₂ and HfSe₂ span ≈ 165 and 95 cm⁻¹, respectively, with both also reaching higher magnitudes of reflectance. Very few materials exhibit such extraordinary magnitudes of Born effective charge and TO-LO splitting in the far-IR, and larger

field splitting can only otherwise be found in ferroelectric oxides^[60,61] and group-IV-VI compounds.^[62,63]

After extracting the thickness and in-plane high-frequency permittivity as fitted parameters from the near-normal FTIR measurements, we then measure the *s*-polarized reflectance in the far-IR (red line, Figure 3c,d) using the grazing angle objective (GAO). Subsequent fitting of the Reststrahlen band is performed using prior reported values for the phonon frequencies^[64,65] as initial values for the parameters. From these measurements we extract the fitted values of the in-plane permittivity: ω_{TO} , ω_{LO} , γ_{TO} , and γ_{LO} . These values are provided in Table 2.

Finally, we measure the *p*-polarized reflectance at the same location (black line, Figure 3c,d). The previously extracted values for the in-plane dielectric function are incorporated into our model, allowing us to focus on the out-of-plane contribution. Note, although our model is successful in matching the overall shape of the reflectance measurements, there remains additional absorptive features that are not accounted for in our model. These features can be identified as offsets between the measured and predicted values in Figure 3 between 350–500 and 225–400 cm⁻¹ for HfS₂ and HfSe₂, respectively. We attribute these features to two-phonon absorption and address them in more detail in Section 2.2.3.

2.2.2. Modeling of the Dielectric Function

For a single IR-active phonon, the permittivity can be derived from a simple harmonic oscillator model resulting in the so-called “TOLO” function:

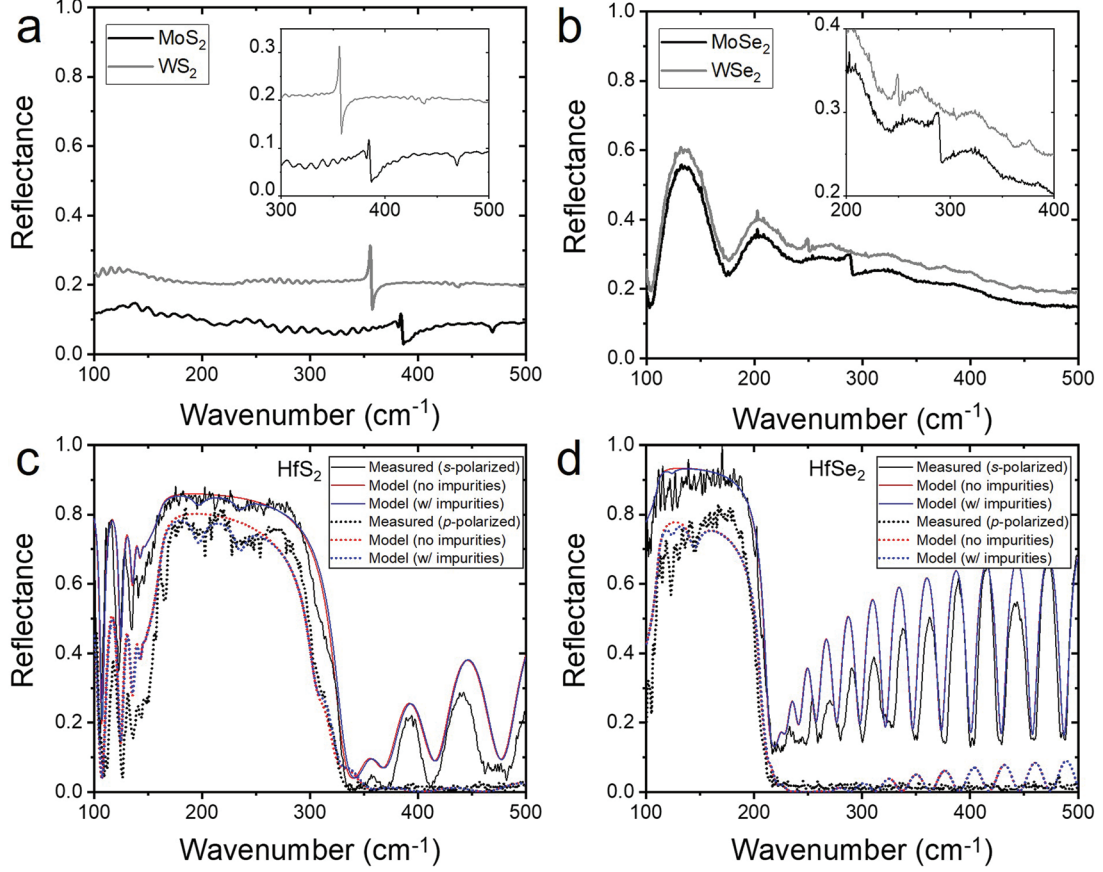


Figure 3. Angle-dependent FTIR reflection measurements of a) MoS₂ and WS₂ and b) MoSe₂ and WSe₂ flakes (offset by 0.05). Inset: zoom of spectra. The p-polarized (dotted) and s-polarized (solid) reflectance spectra of c) HfS₂ and d) HfSe₂. The measured (black) data were fitted using models with (blue) and without (red) impurities. The s-polarized data in (d) is offset by 0.1 for clarity.

$$\varepsilon_{\text{TOLO}}(\omega) = \varepsilon_{\infty, \text{TOLO}} \left(\frac{\omega_{\text{LO}}^2 - \omega_{\text{TO}}^2}{\omega_{\text{TO}}^2 - \omega^2 - i\gamma\omega} \right) \quad (4)$$

where the high frequency permittivity $\varepsilon_{\infty, \text{TOLO}}$ defines the real part of the dielectric function at frequencies above the LO phonon. Although Equation (4) has been successfully used to model the permittivity of several polar materials such as hBN^[22,49] and silicon carbide (SiC),^[66] this approximation fails when anharmonic phonon coupling must be taken into effect as is the case for HfS₂ and HfSe₂. In this case the TO ($\gamma_{\text{TO},i}$) and LO ($\gamma_{\text{LO},i}$) phonon damping for the same phonon branch (i) would

not be assumed to be the same, as in Equation (4). This is true of materials with multiple phonon modes that are close in frequency, such as in perovskites and alkali halides.^[67,68] A more general representation of the TOLO oscillator that allows for independent TO and LO damping has been derived as^[69]

$$\varepsilon(\omega) = \varepsilon_{\infty, \text{TOLO}} \prod_i^n \frac{\omega_{\text{LO},i}^2 - \omega^2 - i\omega\gamma_{\text{LO},i}}{\omega_{\text{TO},i}^2 - \omega^2 - i\omega\gamma_{\text{TO},i}} \quad (5)$$

Note that when $\gamma_{\text{TO},i} = \gamma_{\text{LO},i}$, this reduces to the simple harmonic oscillator model. Yet, for this model to be physical it is necessary that the condition $\sum_i^n (\gamma_{\text{LO},i} - \gamma_{\text{TO},i}) > 0$ be met, otherwise the imaginary permittivity ($\text{Im}(\varepsilon)$) well above the LO phonon frequency would become negative and thus, non-physical for a medium absent of gain. In addition to modeling multiple phonon materials, Equation (5) has also been used to model the absorption due to two-phonon processes in manganese oxide (MnO), magnesium oxide (MgO), and nickel oxide (NiO).^[71] The following section will demonstrate how this model is necessary for reproducing the two-phonon absorption features in HfS₂ and HfSe₂. Therefore, the optical response of HfS₂ and HfSe₂ was modeled using a uniaxial dielectric tensor

Table 2. TOLO model fitting parameters.

	HfS ₂		HfSe ₂	
	In-plane (x,y)		Out-of-plane (z)	
ω_{TO} [cm ⁻¹]	163.6	110.9	180.4	122.1
ω_{LO} [cm ⁻¹]	316.5	203.8	304.4	141.8
γ_{TO} [cm ⁻¹]	8.0	6.9	11.1	9.0
γ_{LO} [cm ⁻¹]	13.3	8.8	15.3	11.9
ε_{∞}	6.30	7.25	10.59	13.77

with Equation (5) being employed to model the dielectric function along the in- and out-of-plane axes.

2.2.3. Two-Phonon Absorption

As stated above, additional absorptive features are observed in the polarized reflectance spectra that are not attributed to the first order optic phonon response. To understand the origin of these features we perform transmission measurements at normal incidence using a very thin, relatively flat sample with the results of this measurement provided in **Figure 4**. The thicknesses of the HfS₂ and HfSe₂ crystals were determined to be 9.9 and 59.3 μm from fitting the near-normal transmission (see Section 4.2.1), respectively. Here we measure at normal incidence, and therefore only the in-plane contribution to the dielectric function is considered. We observe additional features at 350, 470, 505, and 550 cm⁻¹ for HfS₂ that cannot be accounted for by a single TOLO model (Figure 4, dashed line). Similar features have been observed at these frequencies in two-phonon absorption measurements and second order Raman measurements of HfS₂ crystals.^[55,56] We then model each of the two-phonon absorption peaks using the anharmonic TOLO function, as has been implemented in prior work^[71] (Figure 4, black solid line). The two-phonon model is also implemented for the HfSe₂ transmission data (Figure 4d,e). Although the two-phonon absorption features are prominent in the transmission spectrum, their resultant contribution to the dielectric function is weak in comparison to first-order optic phonons. This is seen with the difference in scales between Figure 4b,e,c,f.

2.3. Nanophotonic Resonator

Within the Reststrahlen band, anisotropic materials can exhibit interesting optical properties because of their crystal asymmetry.^[24,25,31,72] The unequal responses between the in-plane isotropic and out-of-plane dielectric tensor components allows for their product to be less than zero ($\text{Re}(\epsilon_{xx,yy}) * \text{Re}(\epsilon_{zz}) < 0$), and under these circumstances the isofrequency surface becomes an open hyperboloid, allowing the material to support high-momenta (\mathbf{k}) hyperbolic phonon polaritons (HPhPs).^[72-75] Conversely, when $\text{Re}(\epsilon_{xx,yy}) * \text{Re}(\epsilon_{zz}) > 0$, the in-plane momentum of light within the material is bound by a closed ellipsoid isofrequency surface. Because $\mathbf{k} \approx \frac{2\pi}{\lambda}$, the HPhPs propagate through the medium with an extremely sub-diffractive wavelength limited by the mode volume, such as the flake thickness or nanostructure size. To quantify the performance of Hf-based TMDs for potential applications in far-IR nanophotonics, we used the extracted permittivity values to calculate the quality (Q)-factor of propagating HPhPs within these materials. The Q-factor compares the polariton propagation length to its modal confinement and is a useful metric of the practicality of a material for nanophotonics.^[30] It is shown here as:

$$Q = \frac{k'}{k''} \quad (6)$$

where k' and k'' are the real and imaginary parts of the propagating wavevector, respectively. The frequency-dependent wavevector can be calculated analytically using the expression:^[73,76]

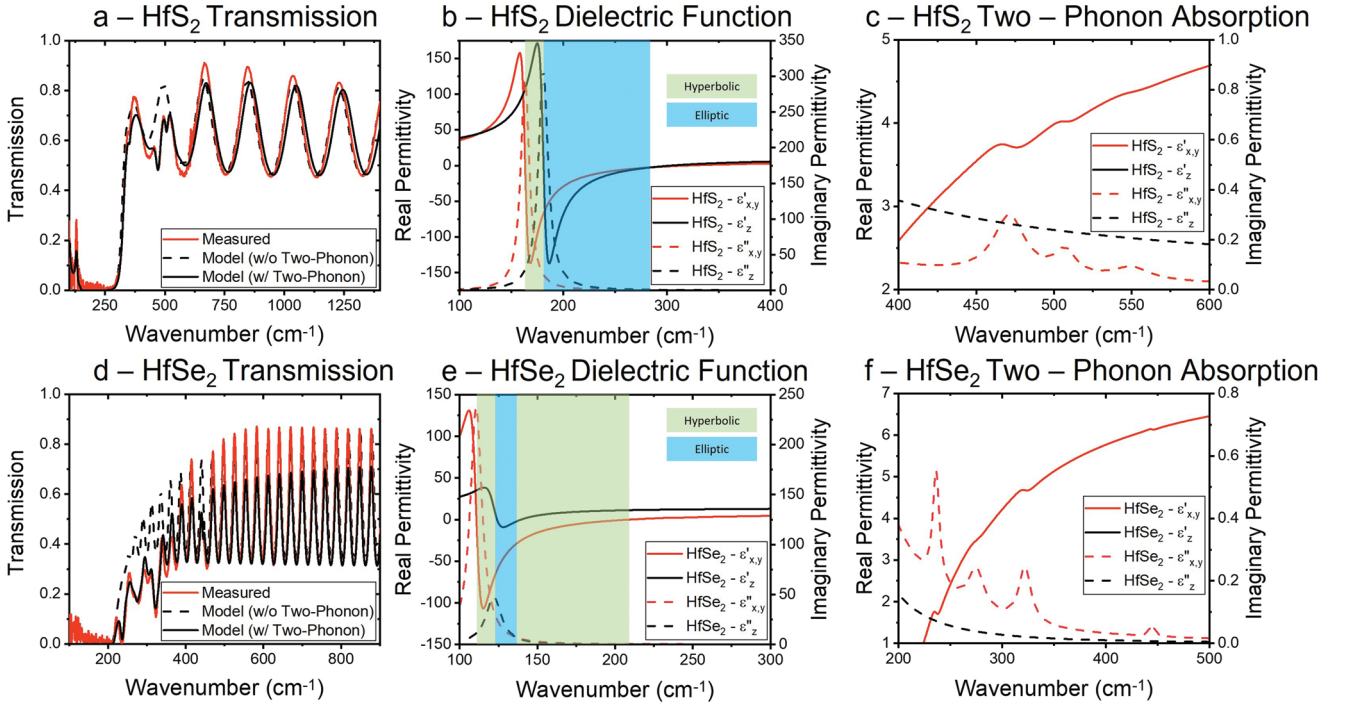


Figure 4. Measured FTIR transmission spectra (solid, red) from flakes of a) HfS₂ and d) HfSe₂. TOLO model fitting with (solid, black) and without (dashed, black) two-phonon absorption. Calculated dielectric function of b) HfS₂ and e) HfSe₂. c,f) Reduced region of (b) and (e) highlighting the two-phonon contribution to the dielectric function.

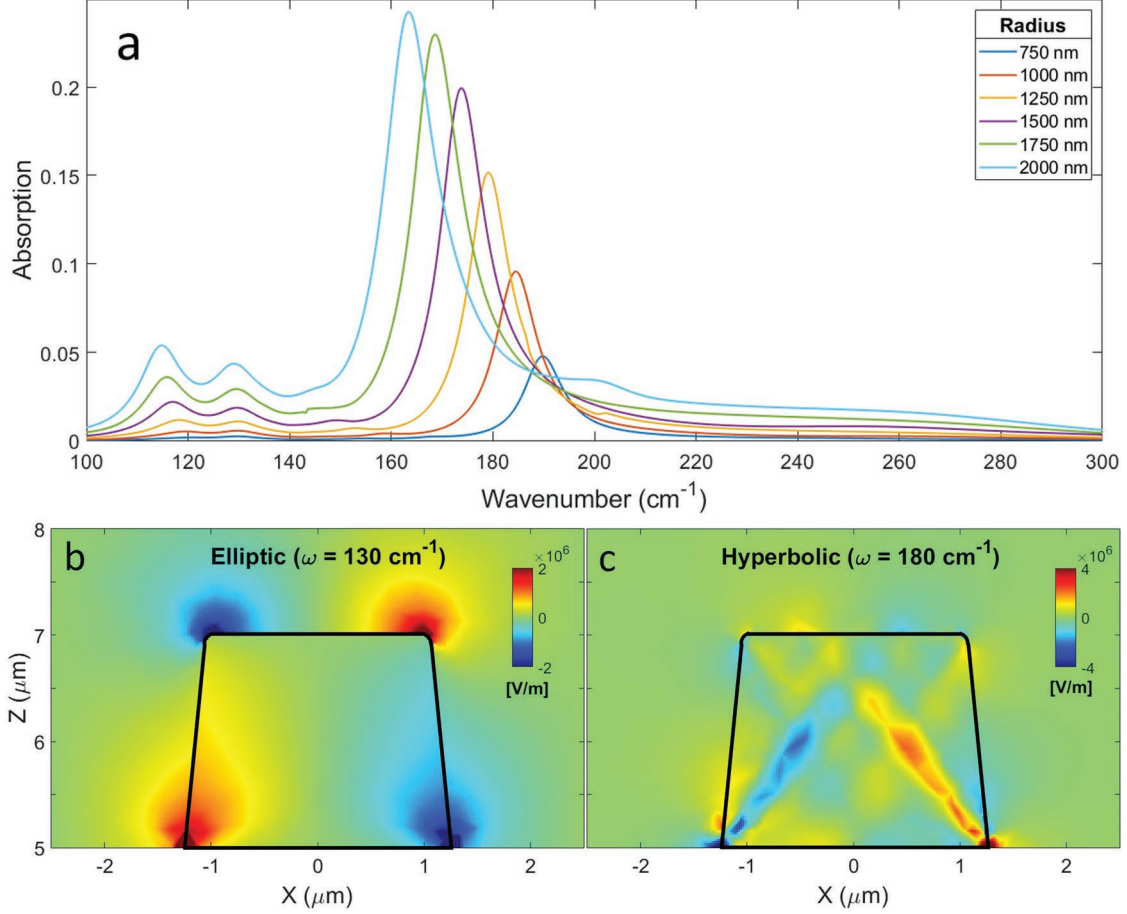


Figure 5. a) Simulated absorbance spectra of HfSe₂ resonator cone with varying radius. Out-of-plane electric field (E_z) cross-sections of a conical HfSe₂ resonator ($R = 1250$ nm) with the b) elliptic and c) hyperbolic frequency ranges. The black line outlines the resonator edges.

$$\bar{\mathbf{k}}(\omega) = k' + ik'' = -\frac{\psi}{d} \left[\arctan\left(\frac{\epsilon_o}{\epsilon_{xx,yy}\psi}\right) + \arctan\left(\frac{\epsilon_s}{\epsilon_{xx,yy}\psi}\right) + \pi l \right];$$

$$\psi = -i \sqrt{\frac{\epsilon_{zz}}{\epsilon_{xx,yy}}} \quad (7)$$

where we assume the thickness (d) of a flake to be 20 nm. ϵ_o and ϵ_s are the complex dielectric functions of surrounding media on either side, however, we use the dielectric function of air for both media. The primary modes ($l = 1$) of HfS₂ and HfSe₂ exhibit peak Q-factors of ≈ 8 and 6, respectively, which is on-par with other naturally occurring hyperbolic materials.^[17] However, these reports are typically from hyperbolic materials with Reststrahlen bands at higher frequencies, which may skew such comparisons. Nonetheless, HfS₂ and HfSe₂ exhibit broad Reststrahlen bands in the mid- to far-IR, 20% and 80% of which are hyperbolic regions, respectively. We examine their potential for nanophotonic devices in the following section.

SPhPs can be confined in flakes with extremely small thicknesses or through fabricated nanostructures. These modes manifest as high extinction peaks within the Reststrahlen band, and with precise control of $\bar{\mathbf{k}}$ through nanofabrication

techniques can be utilized for tunable, high-sensitivity sensing applications. We simulated a periodic array of conical HfSe₂ resonators on a silicon substrate with CST Microwave Studio to calculate the mid- to far-IR polaritonic absorption response under normal incidence. Several modes can be identified in the simulated absorption spectra (**Figure 5a**) between the ω_{TO} and ω_{LO} , most notably those between 160–185 cm^{-1} which lay in the hyperbolic region of the Reststrahlen band. At lower frequencies, two smaller peaks arise just beyond ω_{TO} at 115 and 130 cm^{-1} , respectively. Based on the relationship between $\text{Re}(\epsilon_{xx,yy})$ and $\text{Re}(\epsilon_{zz})$, we see that the lowest and highest frequency peaks lay in the hyperbolic regions, while the 130 cm^{-1} peak sits in the elliptic region. HPhPs propagate within

the material at a fixed angle^[50] $\theta_p(\omega) = \arctan\left(\frac{\sqrt{\epsilon_z(\omega)}}{i\sqrt{\epsilon_{x,y}(\omega)}}\right)$,

depending on the ratio of the polaritonic material and the surrounding dielectric. Localized SPhPs couple with the periodic lattice of resonators and therefore exhibit a field distribution along the edges of the structure. The contrast in modal behavior of localized SPhPs and HPhPs is evident from the simulated out-of-plane electric field (E_z) cross-sections (**Figure 5b,c**). The strong and sharp absorptive feature of the

resonators provides the potential for detecting low-frequency modes with high sensitivity, which is not achievable with most materials.

3. Conclusion

Here, we experimentally measure the far-IR reflectance and transmission of group-IVB TMDs, HfS_2 , and HfSe_2 , and derive their dielectric functions using a harmonic oscillator model. Using first-principles calculations, we also investigate the magnitude of the TO-LO splitting of Hf-based TMDs in the monolayer limit and compare with group-VIB TMD MoS_2 . The ionic character of the bonding between the Hf and chalcogen atoms increases the magnitude of the Born effective charge, and thus creates exceptionally broad Reststrahlen bands that stretch a few orders of magnitude wider than group-VIB TMDs. Finally, we simulate the electromagnetic response of a HfSe_2 conical resonator and find the extraordinary HPhP and localized SPhP modes. Because of the crystal anisotropy, layered Hf-based TMDs can support these hyperbolic modes, which are capable of extremely sub-diffractive wavelengths. This work reveals a class of materials that extends the range of wavelengths that is commonly associated with nanophotonics ($<20\ \mu\text{m}$) into an area that offers potential for rich new physics and applications. We anticipate that this work will attract further attention to research in this spectral range.

4. Experimental Section

Sample Details: All TMDs used in this work were purchased from HQ Graphene. The HfS_2 and HfSe_2 samples were cleaved from bulk crystals (Figure 1) using a razor blade. This allowed to remove smaller crystals that were sufficiently flat while still large enough for microscope reflection measurements. The as-purchased bulk crystals of the remaining TMDs (Figure S1, Supporting Information) were used for FTIR measurements.

FTIR Micro-Spectroscopy Reflectance Measurements: Polarized reflectance spectra were collected using a Hyperion 2000 microscope equipped with a long working distance IR near-normal (Pike, $10\times$, 0.28NA) and grazing angle objectives (GAO) (Bruker, $\approx 55^\circ$) thereby allowing for the in- and out-of-plane components of the dielectric function to be measured and extracted. For the reflection measurements, the spot size ($50\ \mu\text{m} \times 50\ \mu\text{m}$) was set using adjustable apertures in the microscope. At several locations on each sample, the near-normal objective was used to measure the reflection, from which the thickness was extracted. At each measurement location, both near-normal and GAO objectives were used with consistent locations and aperture sizes.

Dielectric Fitting: First, the sinusoidal interference fringes from the near-normal measurements to extract the local flake thickness were fit. The reported fitting parameters (Table 2) were the average of three locations measured on the sample. The high frequency permittivity values using previously reported values were approximated,^[65,66] with the reported values extracted through fitting of the various spectra at high frequencies away from the optic phonons. After extracting the thickness and in-plane high-frequency permittivity, these were used as fixed parameters to extract the out-of-plane permittivity from the GAO measurements.

Computational Details: The phonon dispersions, eigenvectors, and Born effective charges from first principles were calculated, using the density functional perturbation theory formalism^[77] as implemented in the quantum espresso code.^[78,79] For the phonon calculations, the Hellmann-Feynman forces to $0.1\ \mu\text{Ry bohr}^{-1}$ were converged and the 2D implementation of the nonanalytical-term correction for the LO and TO phonons was used.^[58,80] Scalar-relativistic optimized norm-conserving ultrasoft pseudopotentials were used,^[81] and the Perdew–Burke–

Ernzerhof (PBE) form of the generalized gradient approximation (GGA) for the exchange–correlation functional was chosen.^[82] A plane-wave energy cutoff of 65 Ry, a $24 \times 24 \times 1$ k-point mesh and $8 \times 8 \times 1$ q-point mesh to sample the Brillouin zone for all compounds.

Resonator Simulations: Using the extracted anisotropic dielectric function of HfSe_2 , a periodic array of nanophotonic resonator cones on a Si substrate ($5\ \mu\text{m}$) with radius (R) at the base of the resonator and height ($2\ \mu\text{m}$) was modeled. A small (5°) taper was applied in the vertical direction. Maxwell's equation solver CST Microwave Studio was used to simulate the polaritonic response of the resonator from a normally incident plane wave with an electric field oriented along the x -axis. Field monitors were set up at multiple frequencies to capture the frequency-dependent response.

Supporting Information

Supporting Information is available from the Wiley Online Library or from the author.

Acknowledgements

R.A.K. and J.R.N. contributed equally to this work. This work was supported by a Lunar Surface Technology Research Opportunities grant from NASA's Space Technology Research Grants Program (80NSSC 21K0766). J.R.N. acknowledges support from Office of Naval Research Grant N00014-18-12107. J.D.C. acknowledges support by the National Science Foundation under Grant No. 2128240. J.E.A. acknowledges support from the School for Science and Math at Vanderbilt. Work by G.V., D.M.J., and P.N. was partially supported by NSF DMR Grant No. 1905295. C.J.C. was supported by the Department of Energy "Photonics at Thermodynamic Limits Energy Frontier Research Center" under Grant No. DE-SC0019140. D.M.J. was also supported by the Swiss National Science Foundation (SNSF) under Project ID 184259 and the DARPA DRINQS Program under Award No. D18AC00014. P.N. is a Moore Inventor Fellow and gratefully acknowledges support from the Gordon and Betty Moore Foundation through Grant No. GBMF8048. Calculations were performed at the National Energy Research Scientific Computing Center (NERSC), supported by the Office of Science of the U.S. Department of Energy under Contract No. DE-AC02-05CH11231. S.L. acknowledges funding from the National Science Foundation, Division of Materials Research under Award No. 1904760. S.M.S. acknowledges funding from the University of Delaware Summer Research Scholars program.

Conflict of Interest

The authors declare no conflict of interest.

Data Availability Statement

The data that support the findings of this study are available from the corresponding author upon reasonable request.

Keywords

dielectric function, far-infrared, nanophotonics, polaritons, transition-metal dichalcogenides

- [1] S. S. Dhillon, M. S. Vitiello, E. H. Linfield, A. G. Davies, M. C. Hoffmann, J. Booske, C. Paoloni, M. Gensch, P. Weightman, G. P. Williams, E. Castro-Camus, D. R. S. Cumming, F. Simoens, I. Escorcia-Carranza, J. Grant, S. Lucyszyn, M. Kuwata-Gonokami, K. Konishi, M. Koch, C. A. Schmittenmaer, T. L. Cocker, R. Huber, A. G. Markelz, Z. D. Taylor, V. P. Wallace, J. Axel Zeitler, J. Sibik, T. M. Korter, B. Ellison, S. Rea, *et al.*, *J. Phys. D: Appl. Phys.* **2017**, *50*, 043001.
- [2] A. J. Giles, S. Dai, O. J. Glembocki, A. V. Kretinin, Z. Sun, C. T. Ellis, J. G. Tischler, T. Taniguchi, K. Watanabe, M. M. Fogler, K. S. Novoselov, D. N. Basov, J. D. Caldwell, *Nano Lett.* **2016**, *16*, 3858.
- [3] J. M. Pitarke, V. M. Silkin, E. V. Chulkov, P. M. Echenique, *Rep. Prog. Phys.* **2007**, *70*, 1.
- [4] S. S. Dhillon, M. S. Vitiello, E. H. Linfield, A. G. Davies, M. C. Hoffmann, J. Booske, C. Paoloni, M. Gensch, P. Weightman, G. P. Williams, E. Castro-Camus, D. R. S. Cumming, F. Simoens, I. Escorcia-Carranza, J. Grant, S. Lucyszyn, M. Kuwata-Gonokami, K. Konishi, M. Koch, C. A. Schmittenmaer, T. L. Cocker, R. Huber, A. G. Markelz, Z. D. Taylor, V. P. Wallace, J. Axel Zeitler, J. Sibik, T. M. Korter, B. Ellison, S. Rea, *et al.*, *J. Phys. D: Appl. Phys.* **2017**, *50*, 043001.
- [5] B. Liu, H. Bromberger, A. Cartella, T. Gebert, M. Forst, A. Cavalleri, *Opt. Lett.* **2017**, *42*, 129.
- [6] C. Vicario, A. Trisorio, S. Allenspach, C. Rüegg, F. Giorgianni, *Appl. Phys. Lett.* **2020**, *117*, 101101.
- [7] G. T. Papadakis, P. Narang, R. Sundararaman, N. Rivera, H. Buljan, N. Engheta, M. Soljačić, *ACS Photonics* **2018**, *5*, 384.
- [8] W. S. Rodney, *J. Opt. Soc. Am.* **1955**, *45*, 987.
- [9] E. K. Plyler, N. Acquista, *J. Opt. Soc. Am.* **1953**, *43*, 212–1.
- [10] E. K. Plyler, N. Acquista, *J. Opt. Soc. Am.* **1958**, *48*, 668–1.
- [11] J. R. Hollahan, T. Wydeven, C. C. Johnson, *Appl. Opt.* **1974**, *13*, 1844.
- [12] S. S. Ballard, L. S. Combes, K. A. McCarthy, *J. Opt. Soc. Am.* **1953**, *43*, 975.
- [13] A. Boltasseva, H. A. Atwater, *Science* **2011**, *331*, 290.
- [14] D. You, R. R. Jones, P. H. Bucksbaum, D. R. Dykaar, *J. Opt. Soc. Am. B* **1994**, *11*, 486.
- [15] J. Petzelt, T. Ostapchuk, A. Pashkin, I. Rychetský, *J. Eur. Ceram. Soc.* **2003**, *23*, 2627.
- [16] S. S. A. Seo, H. N. Lee, T. W. Noh, *Thin Solid Films* **2005**, *486*, 94.
- [17] T. Low, A. Chaves, J. D. Caldwell, A. Kumar, N. X. Fang, P. Avouris, T. F. Heinz, F. Guinea, L. Martin-Moreno, F. Koppens, *Nat. Mater.* **2017**, *16*, 182.
- [18] H. Ditlbacher, J. R. Krenn, G. Schider, A. Leitner, F. R. Aussenegg, *Appl. Phys. Lett.* **2002**, *81*, 1762.
- [19] S. Foteinopoulou, G. C. R. Devarapu, G. S. Subramania, S. Krishna, D. Wasserman, *Nanophotonics* **2019**, *8*, 2129.
- [20] A. V. Zayats, I. I. Smolyaninov, A. A. Maradudin, *Phys. Rep.* **2005**, *408*, 131.
- [21] J. Zhang, L. Zhang, W. Xu, *J. Phys. D: Appl. Phys.* **2012**, *45*, 113001.
- [22] A. J. Giles, S. Dai, I. Vurgaftman, T. Hoffman, S. Liu, L. Lindsay, C. T. Ellis, N. Assefa, I. Chatzakis, T. L. Reinecke, J. G. Tischler, M. M. Fogler, J. H. Edgar, D. N. Basov, J. D. Caldwell, *Nat. Mater.* **2018**, *17*, 134.
- [23] J. D. Caldwell, L. Lindsay, V. Giannini, I. Vurgaftman, T. L. Reinecke, S. A. Maier, O. J. Glembocki, *Nanophotonics* **2015**, *4*, 44.
- [24] D. M. Juraschek, P. Narang, *Nano Lett.* **2021**, *21*, 5098.
- [25] N. Rivera, T. Christensen, P. Narang, *Nano Lett.* **2019**, *19*, 2653.
- [26] J. Ibáñez, S. Hernández, E. Alarcón-Lladó, R. Cuscó, L. Artús, S. V. Novikov, C. T. Foxon, E. Calleja, *J. Appl. Phys.* **2008**, *104*, 033544.
- [27] A. Mitsuishi, Y. Yamada, H. Yoshinaga, *J. Opt. Soc. Am.* **1962**, *52*, 14.
- [28] R. J. Shiue, D. K. Efetov, G. Grosso, C. Peng, K. C. Fong, D. Englund, *Nanophotonics* **2017**, *6*, 1329.
- [29] K. Ohtani, M. Beck, M. J. Süess, J. Faist, A. M. Andrews, T. Zederbauer, H. Detz, W. Schrenk, G. Strasser, *ACS Photonics* **2016**, *3*, 2280.
- [30] M. He, G. R. S. Iyer, S. Aarav, S. S. Sunku, A. J. Giles, T. G. Folland, N. Sharac, X. Sun, J. Matson, S. Liu, J. H. Edgar, J. W. Fleischer, D. N. Basov, J. D. Caldwell, *Nano Lett.* **2021**, *21*, 7921.
- [31] S. Dai, W. Fang, N. Rivera, Y. Stehle, B.-Y. Jiang, J. Shen, R. Y. Tay, C. J. Ciccarino, Q. Ma, D. Rodan-Legrain, P. Jarillo-Herrero, E. H. T. Teo, M. M. Fogler, P. Narang, J. Kong, D. N. Basov, *Adv. Mater.* **2019**, *31*, 1806603.
- [32] S. Manzeli, D. Ovchinnikov, D. Pasquier, O. V. Yazyev, A. Kis, *Nat. Rev. Mater.* **2017**, *2*, 17033.
- [33] K. F. Mak, C. Lee, J. Hone, J. Shan, T. F. Heinz, *Phys. Rev. Lett.* **2010**, *105*, 136805.
- [34] K. F. Mak, J. Shan, *Nat. Photonics* **2016**, *10*, 216.
- [35] D. Xiao, G. B. Liu, W. Feng, X. Xu, W. Yao, *Phys. Rev. Lett.* **2012**, *108*, 196802.
- [36] W. Long, X. Fan, P. Fang, X. Li, Z. Xi, C. Ruppert, O. B. Aslan, T. F. Heinz, *Nano Lett.* **2014**, *14*, 3335.
- [37] H. M. Hill, A. F. Rigosi, K. T. Rim, G. W. Flynn, T. F. Heinz, *Nano Lett.* **2016**, *16*, 4831.
- [38] X. Xu, W. Yao, D. Xiao, T. F. Heinz, *Nat. Phys.* **2014**, *10*, 343.
- [39] P. K. Chow, R. B. Jacobs-Gedrim, J. Gao, T. M. Lu, B. Yu, H. Terrones, N. Koratkar, *ACS Nano* **2015**, *9*, 1520.
- [40] P. Rivera, H. Yu, K. L. Seyler, N. P. Wilson, W. Yao, X. Xu, *Nat. Nanotechnol.* **2018**, *13*, 1004.
- [41] Y. Chen, J. Xi, D. O. Dumcenco, Z. Liu, K. Suenaga, D. Wang, Z. Shuai, Y. S. Huang, L. Xie, *ACS Nano* **2013**, *7*, 4610.
- [42] A. Krasnok, S. Lepeshov, A. Alú, *Opt. Express* **2018**, *26*, 15972.
- [43] A. Splendiani, L. Sun, Y. Zhang, T. Li, J. Kim, C. Y. Chim, G. Galli, F. Wang, *Nano Lett.* **2010**, *10*, 1271.
- [44] C. Janisch, Y. Wang, D. Ma, N. Mehta, A. L. Elías, N. Perea-López, M. Terrones, V. Crespi, Z. Liu, *Sci. Rep.* **2014**, *4*, 5530.
- [45] C. Huang, S. Wu, A. M. Sanchez, J. J. P. Peters, R. Beanland, J. S. Ross, P. Rivera, W. Yao, D. H. Cobden, X. Xu, *Nat. Mater.* **2014**, *13*, 1096.
- [46] E. Torun, H. Sahin, S. Cahangirov, A. Rubio, F. M. Peeters, *J. Appl. Phys.* **2016**, *119*, 074307.
- [47] S. N. Neal, S. Li, T. Birol, J. L. Musfeldt, *npj 2D Mater. Appl.* **2021**, *5*, 45.
- [48] X. Gonze, C. Lee, *Phys. Rev. B: Condens. Matter Mater. Phys.* **1997**, *55*, 10355.
- [49] J. D. Caldwell, A. V. Kretinin, Y. Chen, V. Giannini, M. M. Fogler, Y. Francescato, C. T. Ellis, J. G. Tischler, C. R. Woods, A. J. Giles, M. Hong, K. Watanabe, T. Taniguchi, S. A. Maier, K. S. Novoselov, *Nat. Commun.* **2014**, *5*, 5221.
- [50] G. Álvarez-Pérez, T. G. Folland, I. Errea, J. Taboada-Gutiérrez, J. Duan, J. Martín-Sánchez, A. I. F. Tresguerres-Mata, J. R. Matson, A. Bylinkin, M. He, W. Ma, Q. Bao, J. I. Martín, J. D. Caldwell, A. Y. Nikitin, P. Alonso-González, *Adv. Mater.* **2020**, *32*, 1908176.
- [51] A. Cingolani, A. Lúgara, F. Lévy, *Phys. Scr.* **1988**, *37*, 389.
- [52] L. Roubí, C. Carlone, *Phys. Rev. B* **1988**, *37*, 6808.
- [53] T. G. Folland, L. Nordin, D. Wasserman, J. D. Caldwell, *J. Appl. Phys.* **2019**, *125*, 191102.
- [54] V. Riede, H. Neumann, F. Lévy, H. Sobotta, *Phys. Status Solidi B* **1983**, *120*, K9.
- [55] A. Cingolani, M. Lúgara, F. Lévy, *Phys. Scr.* **1988**, *37*, 389.
- [56] F. R. Gamble, *J. Solid State Chem.* **1974**, *9*, 358.
- [57] S. P. Ong, W. D. Richards, A. Jain, G. Hautier, M. Kocher, S. Cholia, D. Gunter, V. L. Chevrier, K. A. Persson, G. Ceder, *Comput. Mater. Sci.* **2013**, *68*, 314.
- [58] T. Sohler, M. Gibertini, M. Calandra, F. Mauri, N. Marzari, *Nano Lett.* **2017**, *17*, 3758.

- [59] A. Jain, S. P. Ong, G. Hautier, W. Chen, W. D. Richards, S. Dacek, S. Cholia, D. Gunter, D. Skinner, G. Ceder, K. A. Persson, *APL Mater.* **2013**, *1*, 011002.
- [60] W. Zhong, R. D. King-Smith, D. Vanderbilt, *Phys. Rev. Lett.* **1994**, *72*, 3618.
- [61] K. M. Rabe, P. Ghosez, in *Physics of Ferroelectrics*, Topics in Applied Physics, Vol. 105, Springer, Berlin, Heidelberg **2007**, pp. 117–174.
- [62] A. Svane, N. E. Christensen, M. Cardona, A. N. Chantis, M. van Schilfgaarde, T. Kotani, *Phys. Rev. B* **2010**, *81*, 245120.
- [63] Z. Tian, J. Garg, K. Esfarjani, T. Shiga, J. Shiomi, G. Chen, *Phys. Rev. B: Condens. Matter Mater. Phys.* **2012**, *85*, 184303.
- [64] G. Lucovsky, R. M. White, J. A. Benda, J. F. Revelli, *Phys. Rev. B* **1973**, *7*, 3859.
- [65] A. Laturia, M. L. Van de Put, W. G. Vandenberghe, *npj 2D Mater. Appl.* **2018**, *2*, 6.
- [66] T. E. Tiwald, J. A. Woollam, S. Zollner, J. Christiansen, R. B. Gregory, T. Wetteroth, S. R. Wilson, A. R. Powell, J. Christiansen, R. B. Gregory, T. Wetteroth, S. R. Wilson, *Phys. Rev. B* **1999**, *60*, 11464.
- [67] A. Marronnier, H. Lee, B. Geffroy, J. Even, Y. Bonnassieux, G. Roma, *J. Phys. Chem. Lett.* **2017**, *8*, 2659.
- [68] A. S. Barker, J. J. Hopfield, *Phys. Rev.* **1964**, *135*, A1732.
- [69] C. T. Kirk, *Phys. Rev. B* **1988**, *38*, 1255.
- [70] D. J. Lockwood, G. Yu, N. L. Rowell, *Infrared Phys. Technol.* **2020**, *109*, 103405.
- [71] N. C. Passler, X. Ni, G. Hu, J. R. Matson, G. Carini, M. Wolf, M. Schubert, A. Alù, J. D. Caldwell, T. G. Folland, A. Paarmann, *Nature* **2022**, *602*, 595.
- [72] A. Poddubny, I. Iorsh, P. Belov, Y. Kivshar, *Nat. Photonics* **2013**, *7*, 948.
- [73] S. Dai, Z. Fei, Q. Ma, A. S. Rodin, M. Wagner, A. S. McLeod, M. K. Liu, W. Gannett, W. Regan, K. Watanabe, T. Taniguchi, M. Thiemens, G. Dominguez, A. H. C. Neto, A. Zettl, F. Keilmann, P. Jarillo-Herrero, M. M. Fogler, D. N. Basov, *Science* **2014**, *343*, 1125.
- [74] P. Li, M. Lewin, A. V. Kretinin, J. D. Caldwell, K. S. Novoselov, T. Taniguchi, K. Watanabe, F. Gaussmann, T. Taubner, *Nat. Commun.* **2015**, *6*, 7507.
- [75] G. Hu, J. Shen, C. W. Qiu, A. Alù, S. Dai, *Adv. Opt. Mater.* **2019**, *8*, 1901393.
- [76] A. Fali, S. T. White, T. G. Folland, M. He, N. A. Aghamiri, S. Liu, J. H. Edgar, J. D. Caldwell, R. F. Haglund, Y. Abate, *Nano Lett.* **2019**, *19*, 7725.
- [77] A. Togo, I. Tanaka, *Scr. Mater.* **2015**, *108*, 1.
- [78] K. F. Garrity, J. W. Bennett, K. M. Rabe, D. Vanderbilt, *Comput. Mater. Sci.* **2014**, *81*, 446.
- [79] P. Giannozzi, S. Baroni, N. Bonini, M. Calandra, R. Car, C. Cavazzoni, D. Ceresoli, G. L. Chiarotti, M. Cococcioni, I. Dabo, A. Dal Corso, S. de Gironcoli, S. Fabris, G. Fratesi, R. Gebauer, U. Gerstmann, C. Gougoussis, A. Kokalj, M. Lazzeri, L. Martin-Samos, N. Marzari, F. Mauri, R. Mazzarello, S. Paolini, A. Pasquarello, L. Paulatto, C. Sbraccia, S. Scandolo, G. Sclauzero, A. P. Seitsonen, *et al.*, *J. Phys.: Condens. Matter* **2009**, *21*, 395502.
- [80] T. Sohier, M. Calandra, F. Mauri, *Phys. Rev. B* **2017**, *96*, 075448.
- [81] A. Dal Corso, *Comput. Mater. Sci.* **2014**, *95*, 337.
- [82] G. I. Csonka, J. P. Perdew, A. Ruzsinszky, P. H. T. Philipsen, S. Lebègue, J. Paier, O. A. Vydrov, J. G. Ángyán, *Phys. Rev. B* **2009**, *79*, 155107.